
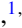







**Incipient antiferromagnetism in the Eu-doped topological insulator  $\text{Bi}_2\text{Te}_3$** 

A. Tcakaev <sup>1</sup>, V. B. Zabolotnyy <sup>1,\*</sup>, C. I. Fornari,<sup>2,3,4</sup> P. Rüßmann <sup>5</sup>, T. R. F. Peixoto,<sup>2,3</sup> F. Stier <sup>1</sup>, M. Dettbarn <sup>1</sup>,  
P. Kagerer,<sup>2,3</sup> E. Weschke,<sup>6</sup> E. Schierle,<sup>6</sup> P. Bencok,<sup>7</sup> P. H. O. Rappl <sup>4</sup>, E. Abramof,<sup>4</sup> H. Bentmann,<sup>2,3</sup>  
E. Goering,<sup>8</sup> F. Reinert,<sup>2,3</sup> and V. Hinkov <sup>1,†</sup>

<sup>1</sup>*Experimentelle Physik IV and Röntgen Research Center for Complex Materials (RCCM), Fakultät für Physik und Astronomie, Universität Würzburg, Am Hubland, D-97074 Würzburg, Germany*

<sup>2</sup>*Experimentelle Physik VII and Röntgen Research Center for Complex Materials (RCCM), Fakultät für Physik und Astronomie, Universität Würzburg, Am Hubland, D-97074 Würzburg, Germany*

<sup>3</sup>*Würzburg-Dresden Cluster of Excellence ct.qmat, Universität Würzburg, Am Hubland, 97074 Würzburg, Germany*

<sup>4</sup>*Laboratório Associado de Sensores e Materiais, Instituto Nacional de Pesquisas Espaciais, São José dos Campos, 12245-970 São Paulo, Brazil*

<sup>5</sup>*Peter Grünberg Institut and Institute for Advanced Simulation, Forschungszentrum Jülich and JARA, D-52425 Jülich, Germany*

<sup>6</sup>*Helmholtz-Zentrum Berlin für Materialien und Energie, Albert-Einstein-Straße 15, D-12489 Berlin, Germany*

<sup>7</sup>*Diamond Light Source, Didcot OX11 0DE, United Kingdom*

<sup>8</sup>*Max-Planck-Institute for Intelligent Systems, Heisenbergstraße 3, 70569 Stuttgart, Germany*



(Received 1 September 2020; revised 6 October 2020; accepted 9 October 2020; published 2 November 2020)

Rare-earth ions typically exhibit larger magnetic moments than transition-metal ions and thus promise the opening of a wider exchange gap in the Dirac surface states of topological insulators. Yet in a recent photoemission study of Eu-doped  $\text{Bi}_2\text{Te}_3$  films, the spectra remained gapless down to  $T = 20$  K. Here we scrutinize whether the conditions for a substantial gap formation in this system are present by combining spectroscopic and bulk characterization methods with theoretical calculations. For all studied Eu doping concentrations, our atomic multiplet analysis of the  $M_{4,5}$  x-ray absorption and magnetic circular dichroism spectra reveals a  $\text{Eu}^{2+}$  valence and confirms a large magnetic moment, consistent with a  $4f^7 \ ^8S_{7/2}$  ground state. At temperatures below 10 K, bulk magnetometry indicates the onset of antiferromagnetic (AFM) ordering. This is in good agreement with density functional theory, which predicts AFM interactions between the Eu impurities. Our results support the notion that antiferromagnetism can coexist with topological surface states in rare-earth-doped  $\text{Bi}_2\text{Te}_3$  and call for spectroscopic studies in the Kelvin range to look for novel quantum phenomena such as the quantum anomalous Hall effect.

DOI: [10.1103/PhysRevB.102.184401](https://doi.org/10.1103/PhysRevB.102.184401)

**I. INTRODUCTION**

In a magnetic topological insulator (TI), a topologically nontrivial electronic band structure in combination with magnetic order leads to exotic states of quantum matter, such as quantum anomalous Hall (QAH) insulators [1–5], axion insulators [6,7], and topological superconductors [8,9]. The QAH effect—which is characterized by dissipationless quantized edge conduction in the absence of external magnetic field and Landau-level formation—remains one of the few topological quantum effects unambiguously observed in recent experiments. This new exotic aspect of condensed-matter physics, first experimentally discovered in Cr-doped  $(\text{Bi}, \text{Sb})_2\text{Te}_3$  TI [1] and later in V-doped systems [2], opens a new avenue for the development of low-dissipation electronics, spintronics, and quantum computation [10]. However, the key conditions for realizing the QAH effect in TI—low bulk carrier densities and long-range ferromagnetic (FM) order with out-of-plane

easy axis—can be achieved only at millikelvin temperatures ( $< 100$  mK).

In past years, great efforts have been made to raise the temperature at which the QAH effect can be observed. Increasing the temperature at least to a few kelvins would already allow the investigation of this effect with more experimental techniques, which could further advance our understanding of it. Unfortunately, the enhanced FM ordering achieved in V-doped  $(\text{Bi}, \text{Sb})_2\text{Te}_3$ , with the Curie temperature ( $T_C$ ) twice as high as that of the Cr-doped sample and about one order of magnitude larger coercivity at the same temperature compared to Cr doping, has little influence on the onset temperature of the QAH effect. Only the recent unconventional doping approaches, such as magnetic codoping of  $(\text{Bi}, \text{Sb})_2\text{Te}_3$  TI with V and Cr, were able to increase the temperature of full quantization to 300 mK [11], while spatially modulated magnetic doping further increased the temperature of the fully quantized QAH effect in Cr-doped  $(\text{Bi}, \text{Sb})_2\text{Te}_3$  up to 0.5 K [12].

Recently, many reports have been published dealing with samples in which rare-earth ions (RE) instead of transition metals (TM) were used as dopants in order to benefit from their large magnetic moments [13–17], which might result in

\*Corresponding author: volodymyr.zabolotnyy@physik.uni-wuerzburg.de

†Corresponding author: hinkov@physik.uni-wuerzburg.de

a larger Dirac gap in the topological surface states (TSS) [18]. The large magnetic moment of the RE elements, originating from the unpaired  $4f$  electrons [19], would also allow for a decrease in the doping concentration and thus the number of defects, leading to a more stable QAH effect at a higher temperature. The highest effective magnetic moment of  $12.6\mu_B$  was observed at 2 K for  $(\text{Dy}_x\text{Bi}_{1-x})_2\text{Te}_3$  with  $x = 0.023$  [20]. However, the magnetic moment of the Dy ions was found to be strongly concentration dependent, in contrast to Gd and Ho dopants in  $\text{Bi}_2\text{Te}_3$  thin films, possessing an effective magnetic moment of  $\sim 7\mu_B$  (close to the maximum free ion value) and of  $\sim 5.15\mu_B$  (half of the theoretical maximum moment), respectively [13]. Despite these large magnetic moments, most investigations found no long-range FM order down to 2 K and thus no gap opening in the TSS [16,21,22]. Only in the case of Dy doping above a critical doping concentration has a sizable gap been reported in angle-resolved photoemission spectroscopy (ARPES), which appears to persist up to room temperature [14]. This gap is observed despite the absence of long-range magnetic order and could originate from short-range FM fluctuations caused by inhomogeneous doping and aggregation of magnetic dopants into superparamagnetic clusters [15], as in the case of Cr-doped  $\text{Bi}_2\text{Se}_3$  [23]. First-principles calculations using density functional theory (DFT) suggest that Eu and Sm ions can introduce stable long-range ferromagnetic order in  $\text{Bi}_2\text{Se}_3$  [24]. This, however, was experimentally confirmed only for Sm ions [25].

Using antiferro- rather than ferromagnetism has also been studied as an avenue to gapped surface states in layered van der Waals compounds. Recently, the realization of such an antiferromagnetic (AFM) topological insulator in  $\text{MnBi}_2\text{Te}_4$  has been reported [26,27]. It is well known that RE chalcogenides such as  $\text{EuTe}$  can exhibit AFM order [28,29]. Therefore it appears promising to take advantage of the larger RE moments to enhance the effect on the TSS in  $\text{Bi}_2\text{Te}_3$ , just like in the case of FM order.

Whereas  $\text{MnBi}_2\text{Te}_4$  is a stoichiometric compound and the AFM order there is intrinsic, here we rely on RE doping of  $\text{Bi}_2\text{Te}_3$  to induce antiferromagnetism, not least to circumvent RE solubility issues. The general feasibility of this approach has been demonstrated for  $\text{Ce}_z\text{Bi}_{2-z}\text{Te}_3$  [30],  $\text{Sm}_z\text{Bi}_{2-z}\text{Te}_3$  [31], and  $\text{Gd}_z\text{Bi}_{2-z}\text{Te}_3$  [32]. As determined by magnetometry [30–32], the onset of AFM interactions is achieved even at low RE concentrations (in the case of Sm,  $z = 0.025$  already suffices). However, x-ray absorption spectroscopy (XAS) and x-ray magnetic circular dichroism (XMCD) investigations addressing the character of the magnetic moments and the impact on the TSS are scarce [33] and limited to temperatures nearly an order of magnitude above the AFM onset temperature, which calls for further investigations.

Here we study  $\text{Eu}_z\text{Bi}_{2-z}\text{Te}_3$  thin films of high structural quality with Eu ions homogeneously incorporated up to a doping level of  $z \sim 0.2$  [34]. We provide a comprehensive investigation of a series of samples with three different Eu concentrations. Combining XAS/XMCD obtained at  $T \sim 10$  K and atomic multiplet calculations allows us to determine the valence state and magnetic moment of the dopants. Using superconducting quantum interference device (SQUID) magnetometry, we observe the onset of antiferromagnetism below about 10 K, which is somewhat unexpected given

the prediction of ferromagnetism in the related chalcogenide  $\text{Eu}_z\text{Bi}_{2-z}\text{Se}_3$ . Furthermore, we characterize the electronic properties by ARPES and resonant photoemission spectroscopy (resPES) at 20 K. Since this is still above the AFM onset temperature, the TSS remains intact and gapless for all Eu doping levels. Nevertheless, our photoemission measurements allowed us to establish a DFT model, which explains the observed in SQUID data onset of antiferromagnetism by the direct overlap of the wave functions of the Eu impurities.

## II. METHODS

### A. Epitaxial film growth and characterization

The samples investigated in this work consist of 100-nm-thick, Eu-doped  $\text{Bi}_2\text{Te}_3$  films, grown by molecular beam epitaxy on  $\text{BaF}_2(111)$  substrates. The Eu doping concentration  $x_{\text{Eu}}$  is defined as the fraction of dopant atoms compared to all atoms in the compound. We estimate  $x_{\text{Eu}}$  from the ratio of  $\text{BEP}_{\text{Eu}}$  and  $\text{BEP}_{\text{Bi}_2\text{Te}_3}$  [34], where BEP is the beam equivalent pressure of the effusion cells. Four different samples were grown with  $x_{\text{Eu}} = 0\%$ , 2%, 4%, and 9%. This would correspond to  $z = 5x_{\text{Eu}} = 0, 0.1, 0.2,$  and  $0.45$  in the chemical formula  $\text{Eu}_z\text{Bi}_{2-z}\text{Te}_3$ , since there are five atoms in total per formula unit. Immediately after the growth, all samples were capped by a 100-nm amorphous Te layer to protect the pristine surface from contamination for the x-ray absorption and photoemission measurements. The capping layer was later removed *in situ* right before the spectroscopic measurements [35]. The detailed growth conditions and a systematic characterization of the film's quality can be found elsewhere [34,36]. X-ray diffraction (XRD) calculations and measurements together with scanning transmission electron microscopy (STEM) images indicate that Eu enters substitutionally on Bi sites at up to 4% of doping, whereas for the 9% Eu-doped sample  $\text{EuTe}$  crystalline clusters of 5–10 nm are formed [34].

### B. X-ray absorption spectroscopy

XAS and x-ray magnetic circular dichroism (XMCD) measurements were carried out using high-field diffractometers at the UE46 PGM-1 beamline, BESSY II, and at beamline I10, Diamond Light Source. Both diffractometers operate under UHV conditions with a base pressure of  $10^{-11}$  mbar. The samples were glued with conducting silver epoxy adhesive onto Cu sample holder and mounted on the cold finger of a helium cryostat. The Te capping layer was mechanically removed *in situ* in the fast-entry chamber at a pressure of  $10^{-9}$  mbar prior to the measurements. The effectiveness of this method to expose a clean sample surface has been demonstrated on  $\text{Bi}_2\text{Te}_3$  previously [35,37].

XAS measurements at Eu  $M_{4,5}$  edges were performed at  $\sim 10$  K and in an external magnetic field of 9 T using circularly polarized light. The degree of circular polarization exceeds 95%. The absorption spectra were measured in the total-electron yield (TEY) mode via the sample drain current normalized to the incoming photon intensity ( $I_0$ ). The TEY is known to be surface sensitive, giving a probing depth of 3–6 nm [38,39]. The XMCD signal was obtained as the difference between two XAS spectra measured in a fixed magnetic

field with incoming photons of opposite helicities in normal incidence geometry. The XAS spectra measured with the helicity vector antiparallel (left) and parallel (right) to the fixed magnetic field were scaled with respect to each other to have the same intensity at energies far from the resonances. Using these scaled intensities  $I_{\text{left}}$  and  $I_{\text{right}}$ , the average XAS is defined as  $I_{\text{avg}} = (I_{\text{left}} + I_{\text{right}})/2$ , while the *normalized* XMCD signal is defined as  $I_{\text{XMCD}} = (I_{\text{left}} - I_{\text{right}})/(I_{\text{left}} + I_{\text{right}})$ . Since only the resonant part of the spectra enters the sum rules, the linear background and the continuum edge jumps were subtracted from the raw spectra.

### C. Angle-resolved photoemission spectroscopy

The photoemission spectra were measured both at laboratory- and synchrotron-based facilities. The laboratory-based ARPES measurements were performed in a UHV system equipped with a Scienta R4000 hemispherical analyzer using He  $I_{\alpha}$  radiation ( $h\nu = 21.2$  eV). The energy resolution was better than 18 meV, and the angular resolution was  $0.2^{\circ}$ . The sample was cooled to 20 K using a liquid He cryostat. The pressure during the measurement never exceeded  $7 \times 10^{-10}$  mbar.

The resonant ( $h\nu \sim 1128$  eV) and off-resonant ( $h\nu = 265$  eV) measurements in the soft x-ray regime were carried out at  $T = 30$  K using the ASPHERE III end station of the P04 beamline at the PETRA III synchrotron facility (DESY, Hamburg, Germany) with a base pressure better than  $2 \times 10^{-10}$  mbar [40]. All studied samples were protected with a Te capping layer, which was removed *in situ* prior to the actual measurement.

### D. Density functional theory calculations

DFT calculations were performed for  $\text{Bi}_2\text{Te}_3$  bulk crystals using the experimental bulk lattice structure [41] into which Eu defects were embedded. The electronic structure was calculated within the local spin density approximation [42] by employing the full-potential relativistic Korringa-Kohn-Rostoker Green's function method (KKR) [43,44] with exact description of the atomic cells [45,46]. The truncation error arising from an  $\ell_{\text{max}} = 3$  cutoff in the angular momentum expansion was corrected for using Lloyd's formula [47]. The Eu defects were embedded self-consistently into the  $\text{Bi}_2\text{Te}_3$  crystal using the Dyson equation in the KKR method [48] and have been chosen to occupy the substitutional Bi position (denoted by  $\text{Eu}_{\text{Bi}}$ ) in the quintuple layers. We included a charge-screening cluster comprising the first three shells of neighboring atoms and structural relaxations around the defect were neglected. All calculations include spin-orbit coupling self-consistently and were performed for an out-of-plane direction of the magnetic moments of the Eu atoms. Correlations within the localized  $4f$  states of Eu were accounted for using an on-site Coulombic correction (LDA + U) [49] for varying values of the parametrization of  $U \in \{0, 7, 8, 9\}$  eV and  $J \in \{0, 0.75, 1.5\}$  eV. To calculate exchange interactions, pairs of Eu impurities were embedded into  $\text{Bi}_2\text{Te}_3$  at different distances for substitutional Bi positions within the same quintuple layer. After the self-consistent impurity embedding calculation, the method of infinitesimal

rotations [50] was used to compute exchange interaction parameters  $J_{ij}$  which correspond to the Heisenberg Hamiltonian  $\mathcal{H} = \frac{1}{2} \sum_{i,j} \hat{\epsilon}_i J_{ij} \hat{\epsilon}_j$ . Here  $\hat{\epsilon}_i$  indicates the direction of the Eu magnetic moment and  $i \neq j$  label the different magnetic Eu atoms. The  $J_{ij}$  parameters were calculated using a numerical smearing temperature of 100 K, which includes the effective contribution of electron scattering due to phonons or intrinsic defects in the  $\text{Bi}_2\text{Te}_3$  host crystal that limit the coherence length of the electron's wave functions. Calculations at higher values of the smearing temperature showed a minor effect on the  $J_{ij}$  values and are therefore not shown explicitly.

### E. Bulk magnetometry

The overall magnetic properties of the  $\text{Eu}_z\text{Bi}_{2-z}\text{Te}_3$  films were measured using bulk-sensitive SQUID magnetometry. SQUID measurements were performed as a function of temperature and magnetic field using a 7-T Quantum Design MPMS 3 SQUID vibrating sample magnetometer (VSM). The diamagnetic contribution from the  $\text{BaF}_2$  substrate was subtracted by high-field linear fitting of  $M(H)$  curves at elevated temperatures (not shown). The temperature dependence of the magnetization was measured in the field-cooled (FC) and zero-field-cooled (ZFC) regimes. In the ZFC measurement, the samples were cooled from room temperature to 2 K without any applied field. After cooling, a magnetic field of 0.1 T was applied perpendicular to the film  $c$  axis, i.e., in plane, and the magnetization was measured upon warming the samples. In the FC measurements the samples were cooled to 2 K in a 0.1-T in-plane field and the data were acquired while heating, similar to ZFC.

## III. RESULTS and Discussions

### A. Eu $M_{4,5}$ XAS and XMCD

Figure 1 shows XAS and XMCD spectra at the Eu  $M_{4,5}$  edges for the 2%, 4%, and 9% Eu-doped  $\text{Bi}_2\text{Te}_3$  samples. The measurements were conducted at a temperature of  $T = 10$  K in an applied field of  $B = 9$  T. The XAS line shapes of all three samples shown in the upper panels are nearly identical and indicate an overwhelming preponderance of  $\text{Eu}^{2+}$  [51,52]. The line shapes of the XMCD spectra shown in the lower panels confirm the  $\text{Eu}^{2+}$  character, corresponding to a  $4f$  electron occupation of  $n_f = 7$  ( $S = 7/2$ ,  $L = 0$ , and  $J = 7/2$ ). The small additional spectral weight observed in the 4% Eu-doped sample [see the inset of Fig. 1(b)] probably stems from  $\text{Eu}^{3+}$ , most likely resulting from surface contamination with  $\text{Eu}_2\text{O}_3$ , as we show in Sec. III C using atomic multiplet calculations.  $\text{Eu}^{3+}$  is nonmagnetic in the Hund's rule ground state ( $S = 3$ ,  $L = 3$ , and  $J = 0$ ) and therefore has no contribution to the XMCD spectrum [53,54]. The electrons of the Eu  $4f$  shell are not directly involved in the formation of chemical bonds, unlike the electrons of the  $5d$  and  $6s$  shells. For this reason, the Eu  $M_{4,5}$  absorption spectrum is typically the same for metals, alloys, and oxides, apart from small differences in the line shape due to the experimental and lifetime broadening [51].

It is worth mentioning that the strength of the normalized dichroism signal shown in the lower panel of Fig. 1, which is directly proportional to the  $4f$  magnetic moment of the Eu ion, slightly decreases upon increasing Eu concentration.

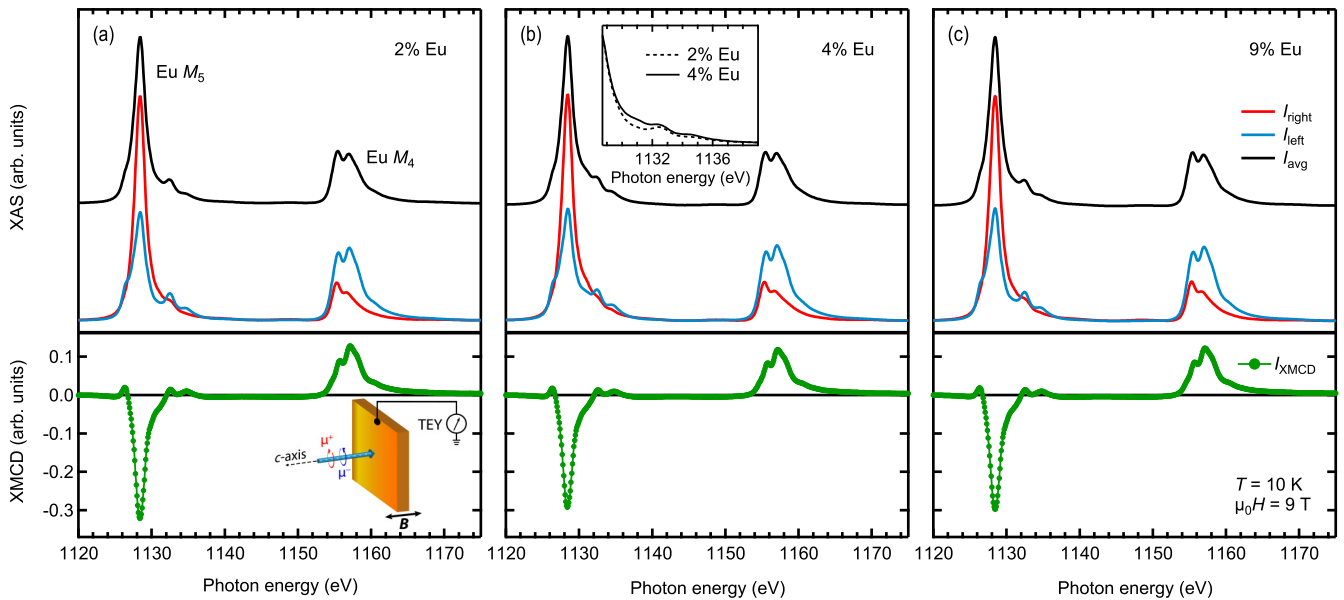


FIG. 1. Experimental Eu  $M_{4,5}$  edges XAS (top) and normalized XMCD (bottom) intensities of (a) 2%, (b) 4%, and (c) 9% Eu-doped  $\text{Bi}_2\text{Te}_3$  thin films measured at  $T = 10$  K in an external magnetic field of 9 T with left-circular ( $I_{\text{left}}$ ) and right-circular ( $I_{\text{right}}$ ) x-ray polarization. The inset in (a) schematically illustrates the experimental geometry. The inset in (b) highlights the additional small spectral weight at the  $M_5$  edge of the 4% Eu-doped sample, which is absent for the other two samples.

The same trend was reported for the concentration dependence of the Dy magnetization in  $\text{Dy}:\text{Bi}_2\text{Te}_3$  films [20]. The XMCD spectra measured at low temperature in remanence (not shown) display no perceptible response for the entire range of studied concentrations of Eu; thus we observe no evidence for a long-range FM order, also consistent with the SQUID results.

Previous XAS and XMCD studies of  $\text{Bi}_2\text{Te}_3$  thin films doped with RE ions other than Eu revealed a 3+ valence of the dopants [13,15,17,20–22,55], in strong contrast with the 2+ valence of the Eu ions found here. This is likely due to the half-filled  $4f$  shell of  $\text{Eu}^{2+}$ ,  $[\text{Xe}] 4f^7$ , having a very stable Hund's rule ground state ( $^8S_{7/2}$ ) with no spin-orbit splitting and a large spin magnetic moment arising from seven unpaired electrons. It is also in line with the observation that the trivalent state is the most stable in oxides, while the divalent state is more stable for the less electronegative chalcogens [34]. Overall, our XAS and XMCD spectra are in good agreement with those previously reported for Eu  $M_{4,5}$  edges [56–58].

Figure 2(a) illustrates the strength of the XMCD signal as a function of external magnetic field measured at 10 K at normal incidence of the x rays, revealing the field-dependent magnetization of Eu ions. The data was obtained by sweeping the out-of-plane applied magnetic field in a range of  $\pm 12$  T at the photon energy of the Eu  $M_5$  edge XMCD peak maximum normalized to the off-resonant region. The shapes of the curves are fairly similar for all three Eu concentrations, with the XMCD strength slightly decreasing by  $\sim 6\%$  when going from 2% to 9% doping level. No evidence for opening of the hysteresis loop was observed for any of the three samples, which points towards the absence of long-range magnetic ordering of Eu moments. Indeed, the magnetization curves can be closely approximated by a Brillouin function [see Fig. 2(a)], which is indicative of paramagnetic behavior.

Besides, all magnetization curves are passing directly through the origin, which once again indicates zero remanent magnetization and coercive field. Similar paramagnetic responses were also observed for Gd, Dy, and Ho ions doped in thin films of  $\text{Bi}_2\text{Te}_3$  [20–22,55]. The comparison of XMCD spectra measured at 10 K and an external magnetic field of 12 T with normal and grazing x-ray beam incidence is shown in Fig. 2(b). No difference between the two spectra can be detected, suggesting no noticeable magnetic anisotropy.

## B. Sum-rule analysis

The spin and orbital magnetic moments, which determine the magnetic properties of our thin films, result from the interplay of the hybridization, spin-orbit coupling (SOC), crystal field (CF), Coulomb and exchange interactions. The highly localized and well-screened  $4f$  electrons of rare-earth elements experience comparatively weak crystal fields ( $\sim 100$  meV) and small hybridizations, with the Coulomb and SOC interactions being the two dominating energies. Owing to this, RE ions can be considered as exhibiting isolated magnetic moments and therefore the materials often show a paramagnetic behavior.

The magnetic moment of the Eu ion can be readily accessed by means of sum-rule analysis. Established by Thole and Carra *et al.*, the sum rules relate the ratio of integrated XAS and XMCD spectra to the expectation values of spin and orbital angular momenta [59,60]. For  $3d \rightarrow 4f$  transitions the sum rules are given by

$$\langle L_z \rangle = \left( \frac{2q}{r} \right) n_h, \quad (1)$$

$$\langle S_z \rangle = - \left( \frac{5p - 3q}{2r} \right) n_h - 3 \langle T_z \rangle. \quad (2)$$

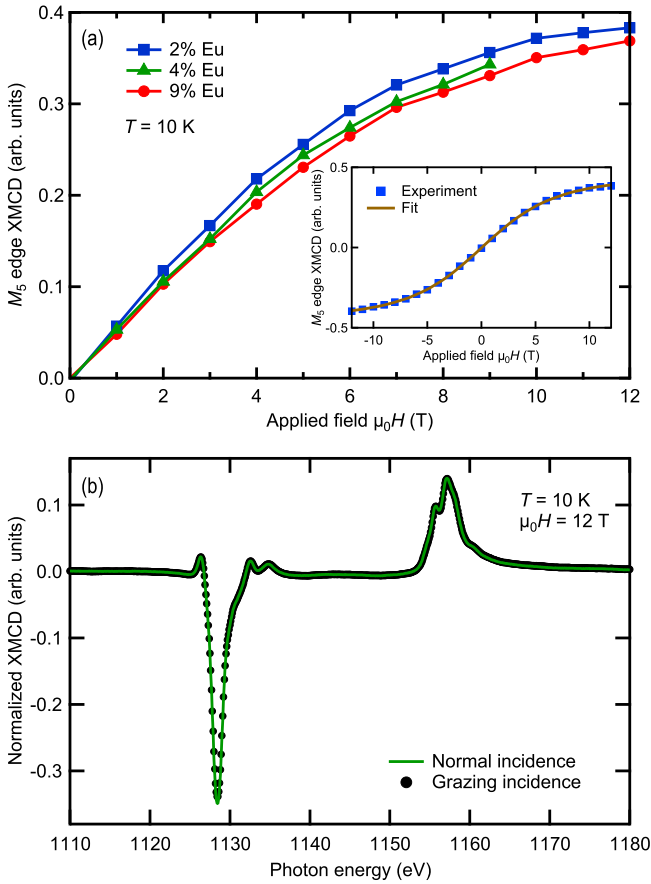


FIG. 2. (a) Magnetic field dependence of the  $M_5$  edge XMCD TEY signal for 2% Eu-doped (squares), 4% Eu-doped (triangles), and 9% Eu-doped (circles)  $\text{Bi}_2\text{Te}_3$  measured at  $T = 10$  K, at normal incidence of the x rays. The inset exemplarily illustrates the 2% Eu-doped sample fitted with a Brillouin function (brown line). (b) Normalized XMCD measured at 10 K in an external magnetic field of 12 T for normal incidence of the x rays, as well as for  $70^\circ$  off-normal, i.e., nearly grazing incidence, showing no noticeable anisotropy.

As indicated in Fig. 3(a),  $p$  is the integrated intensity of  $(I_{\text{left}} - I_{\text{right}})$  over the  $M_5$  edge,  $q$  is the same integral taken over the entire range encompassing the  $M_5$  and  $M_4$  edges, and  $r$  is the intensity of  $(I_{\text{left}} + I_{\text{right}})$  integrated over the same range as  $q$ . Furthermore,  $n_h$  stands for the number of  $4f$  holes, and  $\langle T_z \rangle$  is the expectation value of the intra-atomic magnetic dipole operator [60]. Using the above equations, one can estimate the orbital and spin magnetic moments as  $m_{\text{orb}} = -\langle L_z \rangle \mu_B$  and  $m_{\text{spin}} = -2\langle S_z \rangle \mu_B$ , respectively. To estimate the required value of  $\langle T_z \rangle$ , we performed an atomic multiplet calculation for  $\text{Eu}^{2+}$  and found it to be negligibly small  $\langle T_z \rangle = -0.004\hbar$ , in good agreement with previously reported values [61]. The number of holes  $n_h$  was taken to be 7 for the Eu  $4f^7$  valence shell. Similarly to our previous publication, we apply a correction factor to the spin sum rule in order to compensate for the  $jj$  mixing between the  $3d_{5/2}$  and  $3d_{3/2}$  core levels [37]. However, for  $\text{Eu}^{2+}$  the correction factor has a rather small value of 1.06, indicating a low mixing of these two manifolds.

TABLE I. Spin, orbital, and saturation magnetic moments estimated using XMCD sum rules for Eu  $M_{4,5}$  absorption edges (in units of  $\mu_B$ ). The scaling factor  $\mathcal{C}$  was obtained from the fit of the XMCD magnetic field dependence with a Brillouin function, as shown in Fig. 2.

Sample	$m_{\text{spin}}$	$m_{\text{orb}}$	$m_{\text{spin}}^{\text{sat}}$	$\mathcal{C}$
2% Eu	$5.23 \pm 0.21$	$-0.09 \pm 0.06$	$6.64 \pm 0.29$	$1.27 \pm 0.02$
4% Eu	$4.85 \pm 0.20$	$-0.06 \pm 0.11$	$6.35 \pm 0.47$	$1.31 \pm 0.08$
9% Eu	$5.03 \pm 0.22$	$0.02 \pm 0.07$	$6.79 \pm 0.39$	$1.35 \pm 0.05$

Since the extracted magnetic moments depend in a nontrivial way on the input parameters controlling the normalization and background subtraction procedures, as well as on the integration energy range [ $E_0$ ,  $E_{\text{cutoff}}$ , and  $E_1$  shown in Fig. 3(a)] and  $n_h$ , we vary the input parameters in a random and uncorrelated way within the assumed confidence intervals and examine how the final results get distributed, see Figs. 3(b) and 3(c). In this way we are able to account for possible conjoined effects of the input parameters and produce fair estimates for the uncertainties in  $m_{\text{spin}}$  and  $m_{\text{orb}}$  [37].

Further, we notice that due to the paramagnetic behavior of the Eu magnetization, the external magnetic field of 9 T was not sufficient to saturate the magnetic moments at  $T = 10$  K, the temperature at which the data for the sum-rule analysis were collected. Therefore we fit the magnetic field dependence of the  $M_5$  edge XMCD signal with a Brillouin function,  $B_J(x)$  with  $x = \frac{gJ\mu_B B}{k_B(T - \theta_p)}$  [62], as illustrated in the inset of Fig. 2(a), which accounts for the finite temperature, and determine the scaling constant  $\mathcal{C} = M(T = 0, B = +\infty)/M(T, B)$ . This scaling constant is later used to obtain the magnetic moment at saturation by its value at finite  $T$  and  $B$ . The fit with Brillouin function indicates that to reach 99% of the full saturation moment at  $T = 10$  K, one would have to apply an external magnetic field of about 50 T.

The results of the sum-rules application for the Eu ions are listed in Table I. As expected for  $\text{Eu}^{2+}$  with its half-filled  $4f$  shell, the orbital magnetic moment  $m_{\text{orb}}$  is almost completely quenched for all three concentrations. The values of the saturation spin magnetic moment  $m_{\text{spin}}^{\text{sat}}$ , within the error bars, are also consistent with the  $^8S_{7/2}$  ground state for the 2% and 9% Eu-doped samples, while for the 4% doped sample there is some reduction, which could be explained by a nondichroic contribution coming from the  $\text{Eu}^{3+}$  contamination. In the following section we will compare the moments obtained with the sum-rule analysis with those obtained by atomic multiplet theory.

### C. Atomic multiplet calculations

Theoretical XAS and XMCD spectra for the  $M_{4,5}$  ( $3d \rightarrow 4f$ ) absorption of  $\text{Eu}^{2+}$  and  $\text{Eu}^{3+}$  ions were calculated using crystal field multiplet theory (CFT) in the framework developed by Thole *et al.* [51]. The calculation takes into account all the  $3d - 4f$  and  $4f - 4f$  electronic Coulomb interactions, as well as the spin-orbit coupling on every open shell of the absorbing atom. The initial values for the Slater integrals were obtained using Cowan's atomic Hartree-Fock (HF) code with

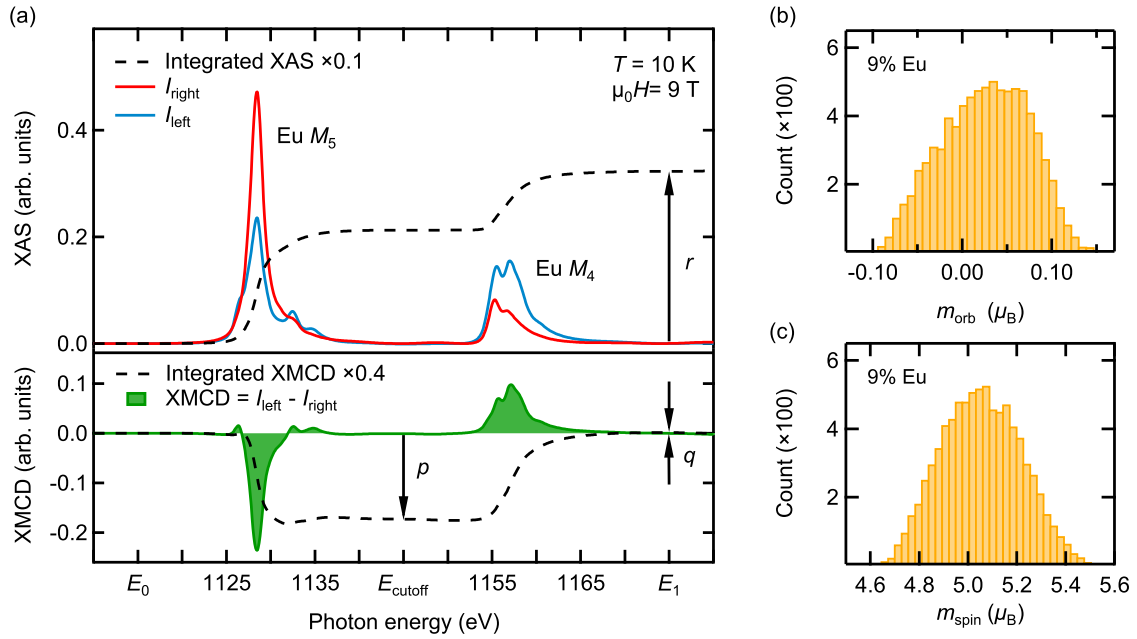


FIG. 3. Sum-rule analysis for the 9% Eu-doped sample. (a) Left- and right-circularly polarized XAS spectra of the Eu  $M_{4,5}$  edges, obtained after the background corrections described in Sec. II ( $I_{\text{left}}$ , solid, light blue line, and  $I_{\text{right}}$ , solid dark red line), along with the corresponding XMCD data (solid green line, lower panel). The dashed lines show the total integrated XAS and XMCD spectral weight, respectively. The arrows mark the values of  $r$ ,  $p$ , and  $q$  used in Eqs. (1) and (2).  $E_0$  and  $E_1$  denote the onset and the end energy of the entire  $M_{4,5}$  edges, and  $E_{\text{cutoff}}$  denotes the energy separating the  $M_4$  and  $M_5$  contributions. (b, c) Distribution of  $m_{\text{orb}}$  and  $m_{\text{spin}}$ , respectively, obtained after application of the sum rules 8192 times, for different sets of fitting parameters, as described in the main text.

relativistic corrections [63]. Their optimized values together with the spin-orbit coupling constants used in the calculations for the  $\text{Eu}^{2+} 3d^{10}4f^7$  and  $\text{Eu}^{3+} 3d^{10}4f^6$  initial state and for the  $\text{Eu}^{2+} 3d^9 4f^8$  and  $\text{Eu}^{3+} 3d^9 4f^7$  final state are shown in Table II. The HF values of the direct Slater integrals  $F$ , determining the size of the electron-electron repulsion, were reduced to 84%, while those of the exchange Slater integrals  $G$  were reduced to 74%, to account for intra-atomic screening effects [51]. These scaling parameters of Slater integrals were found to be the optimal values for the Eu  $M_{4,5}$  XAS and XMCD spectra, accurately describing the total spread of the lines in the  $3d_{3/2}$  and  $3d_{5/2}$  peaks. The strength of the spin-orbit coupling in the  $d$  shell was scaled down to 99% for a better match to the experimental data. The relaxation of atomic orbitals upon the  $3d \rightarrow 4f$  excitation leads to a slight change in the Slater integrals and the spin-orbit coupling constants  $\zeta_{4f}$  and  $\zeta_{3d}$ . To account for this effect, we used separate sets of these parameters for the initial and final states. As expected, this resulted in a better agreement between the

calculated and experimental spectra. The hybridization effect between the localized  $f$  electrons and conduction electrons is considered to be weak [64] and was therefore neglected in the calculations. In our calculation we consider only Eu atoms that substitute Bi in  $\text{Bi}_2\text{Te}_3$ , which entails  $C_{3v}$  symmetry of the CF. Since the nearest six Te atoms form almost a perfect octahedron, one could have used  $O_h$  symmetry, but we disregard the CF altogether. This simplification is justified by the effective shielding of the external electrostatic potential by the outer  $5s$  and  $5p$  shells, so the CF splitting in the  $f$  shell turns out to be small ( $\sim 100$  meV) compared to the experimental resolution (120–250 meV) [65] and can be neglected in the current consideration. For comparison, in EuO with its divalent state of Eu, the CF value of 175 meV was obtained by means of multiplet calculations of anisotropic x-ray magnetic linear dichroism [66].

Calculations were performed using the QUANTY software package for quantum many-body calculations developed by Haverkort *et al.* [67], which is based on second

TABLE II. Optimized CFT parameters for  $\text{Eu}^{2+}$  and  $\text{Eu}^{3+}$  ions used in the atomic multiplet calculation (in units of eV). The best fit yields a reduction of the  $F$  and  $G$  Slater integrals to 84% and 74% of their Hartree-Fock values, respectively.

Ion	State	Configuration	$F_{ff}^{(2)}$	$F_{ff}^{(4)}$	$F_{ff}^{(6)}$	$\zeta_{4f}$	$F_{df}^{(2)}$	$F_{df}^{(4)}$	$G_{df}^{(1)}$	$G_{df}^{(3)}$	$G_{df}^{(5)}$	$\zeta_{3d}$
$\text{Eu}^{2+}$	Initial	$3d^{10}4f^7$	10.913	6.807	4.886	0.160	6.728	3.056	4.066	2.379	1.642	11.052
	Final	$3d^9 4f^8$	11.579	7.238	5.200	0.187	7.347	3.389	4.548	2.664	1.840	11.295
$\text{Eu}^{3+}$	Initial	$3d^{10}4f^6$	11.826	7.422	5.340	0.175	7.270	3.330	4.446	2.603	1.797	11.048
	Final	$3d^9 4f^7$	12.428	7.812	5.624	0.202	7.866	3.656	4.922	2.885	1.993	11.291

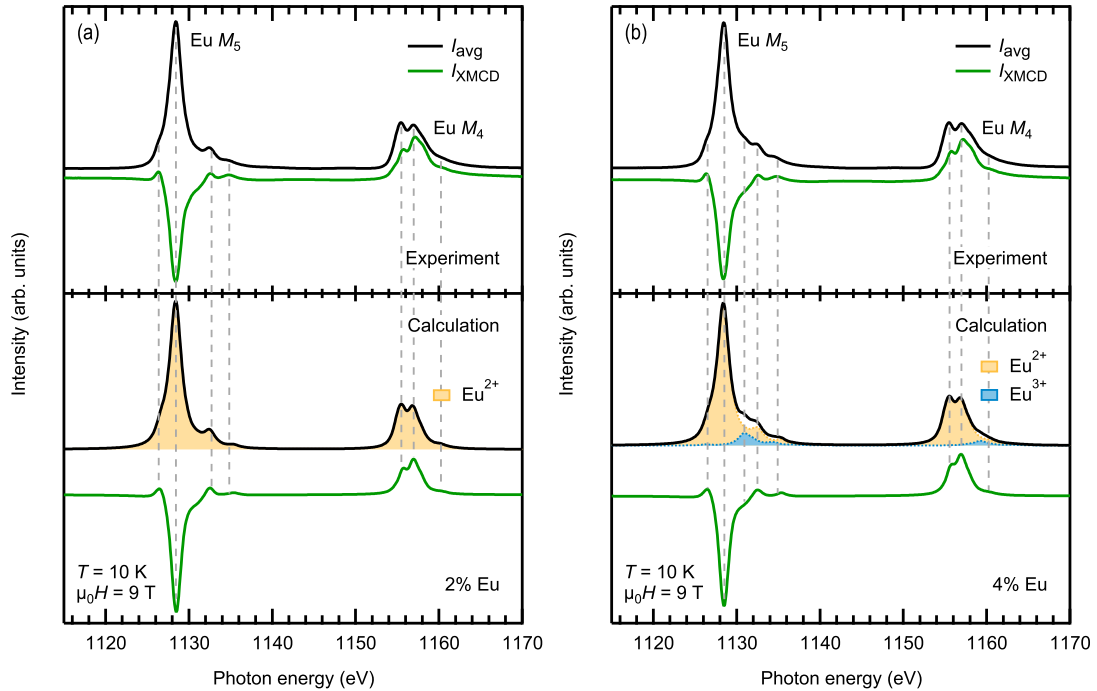


FIG. 4. Top panel: Experimental Eu  $M_{4,5}$  XAS averaged over the two polarizations and XMCD spectra of (a) 2% and (b) 4% Eu-doped  $\text{Bi}_2\text{Te}_3$  measured at  $T = 10$  K in an external magnetic field of 9 T. Bottom panel: Calculated average XAS and XMCD spectra for  $\text{Eu}^{2+}$  and  $\text{Eu}^{3+}$  obtained by atomic multiplet theory. The dashed vertical lines are drawn as a guide to the eye, highlighting the position of particular features in the spectra.

quantization and the Lanczos recursion method to calculate Green's functions through avoiding the explicit calculations of the final states. The spectral contributions of the split ground-state terms to the absorption spectra were weighted using a Boltzmann factor corresponding to the experimental temperature of  $T \approx 10$  K. Since the experiments were performed in an external magnetic field of 9 T, this was also included in the calculation. To account for the instrumental and intrinsic lifetime broadening, the calculated spectra were convoluted with a Gaussian function with a standard deviation  $\sigma = 0.2$  eV and with an energy-dependent Lorentzian profile of 0.4–0.6 eV FWHM. The calculated spectra of  $\text{Eu}^{2+}$  and  $\text{Eu}^{3+}$  are linearly superposed with the relative energy position and the relative intensity as adjustable parameters.

Figure 4 shows the comparison of calculated XAS and XMCD spectra for the 2% and 4% Eu-doped samples with experimental data obtained at  $T = 10$  K and  $B = 9$  T. We obtain good agreement between experiment and theory, reproducing all essential spectral features and their relative energy positions denoted by vertical dashed lines. This good agreement for the RE  $M_{4,5}$  edges is partly due to the CFT being ideally suited to describe transitions into well-localized  $4f$  states. The calculations for the 2% and 9% Eu-doped samples [see Fig. 4(a)] indicate that it is sufficient to consider only divalent Eu to reproduce the experimental spectra with no detectable presence of  $\text{Eu}^{3+}$ . On the other hand, the best fit to the experimental data for the 4% Eu-doped sample, shown in the lower panel of Fig. 4(b), is obtained with spectral contributions of 93% from  $\text{Eu}^{2+}$  and 7% from  $\text{Eu}^{3+}$  ions. In the calculation the  $\text{Eu}^{3+}$  spectrum was shifted by 2.5 eV towards higher energies compared to that for the  $\text{Eu}^{2+}$  state, which is consistent with

previous works [52,54,68,69]. According to Hund's rules, one would expect a nonmagnetic ground state of  $\text{Eu}^{3+} \ ^7F_0$  ( $S = 3$ ,  $L = 3$ ,  $J = 0$ ). Due to the nonvanishing interaction with the external magnetic field as compared to the spin-orbit interaction, there is a tiny magnetic moment in the  $4f$  shell. However,  $\text{Eu}^{3+}$  XMCD is much smaller compared to  $\text{Eu}^{2+}$ . The magnetization arising from the Van Vleck paramagnetism of  $\text{Eu}^{3+}$  due to the admixture of low-lying excited states is also small, with a negligible contribution to the XMCD spectral shape.

The calculations, which were carried out for  $\text{Eu}^{2+}$  with the same temperature ( $T = 10$  K) and external magnetic field ( $B = 9$  T) as in the experiment, result in a finite orbital moment  $m_z^{\text{orb}} = g_l \langle L_z \rangle = 0.02 \mu_B$ , a spin magnetic moment  $m_z^{\text{spin}} = g_s \langle S_z \rangle = 6.10 \mu_B$ , and an effective magnetic moment  $m_z^{\text{eff}} = \sqrt{\langle \mu^2 \rangle} = 7.91 \mu_B$ . The nonvanishing orbital moment is due to the finite spin-orbit interaction in the  $4f$  shell as compared to the Coulomb interaction. As for the  $\text{Eu}^{3+}$ ,  $m_z^{\text{orb}} = -0.07 \mu_B$  and  $m_z^{\text{spin}} = 0.15 \mu_B$ . Taking into account the experimental temperature uncertainty, we obtain  $m_z^{\text{spin}} = (6.10 \pm 0.44) \mu_B$ , which is reasonably close to the XMCD sum-rule results listed in Table I. Sum rules and atomic multiplet calculations also yield similar results for  $m_z^{\text{orb}}$ . Possible causes for the small deviation of the sum-rules-extracted spin magnetic moments from the multiplet calculations are nonmagnetic contributions of the Eu sites or noncollinear alignment of the Eu ions in the paramagnetic phase, as well as partial antiferromagnetic coupling between the Eu ions [28,70].

Figure 5 shows the magnetic field dependence of the CFT-calculated  $m_z^{\text{spin}}$  for  $\text{Eu}^{2+}$ . Within the error bars resulting

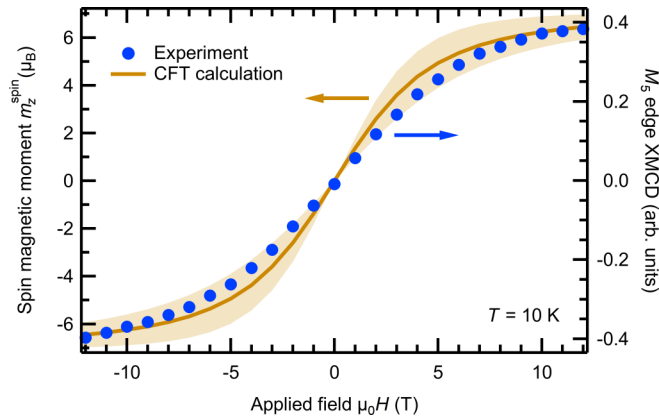


FIG. 5. Magnetic field dependence of the CFT-calculated spin magnetic moment  $m_z^{\text{spin}}$  (solid line) and of the experimental  $M_5$  edge XMCD TEY signal for the 2% Eu-doped  $\text{Bi}_2\text{Te}_3$  thin film (full circles) measured at  $T = 10$  K at normal incidence of the x rays. The shaded area indicates the error, as estimated in the main text.

from experimental temperature uncertainty, it well reproduces the experimental field-dependent magnetization of Eu ions in  $\text{Bi}_2\text{Te}_3$  at  $T = 10$  K.

#### D. Te $M_{4,5}$ and Bi $N_{4,5}$ XAS and XMCD

In our recent work comparing the magnetic properties of V- and Cr-doped  $(\text{Bi}, \text{Sb})_2\text{Te}_3$  [37], we demonstrated a significant XMCD signal detected at nominally nonmagnetic Sb and Te host atoms due to the strong  $pd$  hybridization between TM dopants and the host material. Here, in the case of Eu-doped  $\text{Bi}_2\text{Te}_3$ , we have also checked for dichroism at Bi and Te sites. Figure 6 displays the XAS and XMCD measurements at the Bi  $N_{4,5}$  and Te  $M_{4,5}$  absorption edges at a temperature of 5 K in an applied magnetic field of 2 T. There is no spin polarization detectable on the Te and Bi sites for any dopant concentration. This indicates that a possible magnetic interaction between Eu atoms is not mediated through Te or Bi by means of some sort of indirect exchange.

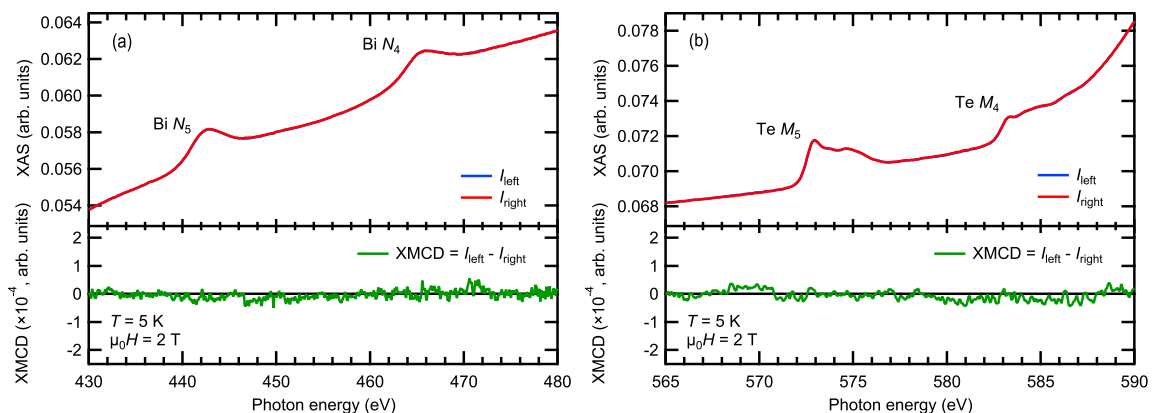


FIG. 6. Normalized (a) Bi  $N_{4,5}$  and (b) Te  $M_{4,5}$  XAS (top panel) and XMCD (bottom panel) intensities of the 2% Eu-doped sample measured at 5 K in an external magnetic field of 2 T.

#### E. Bulk magnetometry results

The bulk magnetic properties of our samples were investigated using a laboratory-based SQUID magnetometer. Figure 7 shows the field-cooled magnetic susceptibility  $\chi$  as a function of temperature for all three samples measured in an in-plane applied magnetic field of 100 mT. The inset compares the inverse magnetic susceptibilities  $1/\chi$  for all three samples as a function of temperature. The magnetic susceptibility data can be fitted using the Curie-Weiss law  $\chi = \chi_0 + C/(T - \theta_p)$  (solid black lines), but there are deviations from this law below about 10 K. Here  $\chi_0$  represents a temperature-independent contribution,  $C$  is the Curie constant, and  $\theta_p$  is the Weiss temperature. Our fit reveals negative Weiss temperatures  $\theta_p = -7.8$  K,  $-2.1$  K, and  $-5.6$  K for the 2%, 4%, and 9% Eu-doped samples, respectively. These negative values suggest an existence of AFM ordering at low temperatures, below the temperature of about 10 K at which the XMCD data was acquired. A similar behavior was also reported for Gd-, Dy-, and Ho-doped  $\text{Bi}_2\text{Te}_3$  thin films [13]. For the Gd-doped single crystals  $\text{Gd}_x\text{Bi}_{2-x}\text{Te}_3$  with  $x = 0.20$ , the magnetic phase transition from a PM phase to an AFM phase was reported to occur at the Néel temperature  $T_N = 12$  K [32].

Whereas a negative Weiss temperature  $\theta_p$  is a strong indication of antiferromagnetism, the value of  $-\theta_p$  frequently deviates substantially from the Néel temperature  $T_N$  [71,72]. However, antiferromagnets typically exhibit a cusp feature near the temperature at which  $\chi(T)$  starts deviating from the Curie-Weiss law (Fig. 7). The Néel temperature can be estimated from the position of this cusp [32,71,72]. For the 2% Eu-doped sample we find  $T_N \approx 6.0$  K, while for the 4% and 9% samples the Néel temperature is about 9.0 and 10.5 K. This seems to be the expected simple monotonic behavior as a function of Eu concentration. Increased concentration results in a higher interaction strength due to the shorter average distances between Eu ions, and hence in a higher Néel temperature.

At even lower temperatures,  $\chi(T)$  increases again and tends to approach the Curie-Weiss curve to some extent, as was also observed for Ce and Gd doping [30,32]. We attribute this to the paramagnetism usually present in strongly dilute



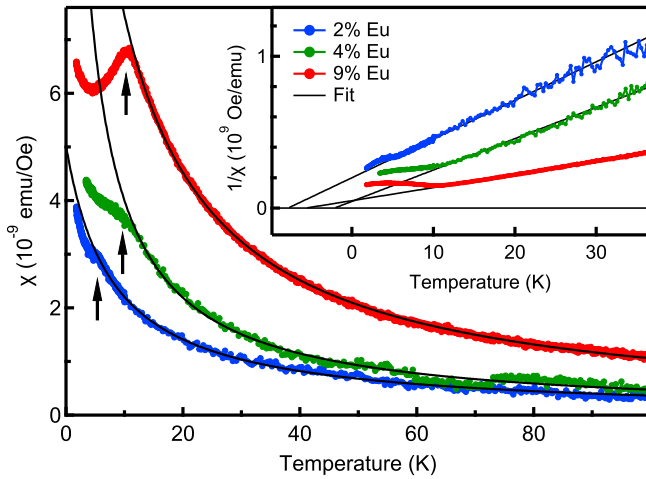


FIG. 7. Field-cooled magnetic susceptibility  $\chi$  for 2% Eu-doped (solid black), 4% Eu-doped (solid red), and 9% Eu-doped (solid blue)  $\text{Bi}_2\text{Te}_3$  in a 2–100 K temperature range. The arrows indicate the Néel temperature estimated from the cusp in the  $\chi(T)$  curves. In the inset, a comparison of the inverse magnetic susceptibility for the corresponding samples is shown at low temperatures from 2 to 35 K. The black solid lines represent linear Curie-Weiss fits to the experimental data.

systems in which some magnetic ions are statistically too far away from others to couple antiferromagnetically. This interpretation is supported by the observation that the paramagnetic component is particularly strong for the 2% sample, which is the most dilute one. Finally, some paramagnetic impurities might potentially also be present in the substrate.

As we have previously discussed [34], the 9% sample, stretching the solubility limit of Eu in  $\text{Bi}_2\text{Te}_3$ , is prone to Eu inhomogeneities and clustering. Therefore it is possible that the much more pronounced cusp feature in the case of the 9% sample is related to AFM EuTe crystalline clusters. For example, for Eu-doped GeTe bulk crystals, AFM order was

observed due to EuTe clusters at  $T_N \approx 11$  K [73]. In fact, EuTe is a well-known magnetic semiconductor and a prototypical Heisenberg antiferromagnet below  $T_N = 9.8$  K [29].

## F. Electronic properties

To study the effect of Eu dopants on the electronic structure of  $\text{Bi}_2\text{Te}_3$ , we have performed extensive laboratory- and synchrotron-based photoemission measurements. The laboratory-based angle-resolved spectra (ARPES) were taken at 20 K using He  $I_\alpha$  radiation ( $h\nu = 21.2$  eV) right after mechanical removal of the Te capping layer. In Figs. 8(a)–8(d) we show the data for all samples, including the undoped reference sample. While the M-shaped bulk valence band (VB) and the bulk conduction band (CB) can be seen for all samples, the topological surface state (TSS) is clearly observed only up to 2% doping. For the higher levels, the spectra are getting blurred because of the increased structural disorder [34]. To better highlight the bands, we supplement these data with the second derivative plots shown in Figs. 8(e)–8(h) [74,75]. The gapless TSS can now be seen for all doping levels. The estimated Fermi velocity ranges from  $2.55$  eV  $\text{\AA}$  ( $3.9 \times 10^5$  m/s) to  $2.63$  eV  $\text{\AA}$  ( $4.0 \times 10^5$  m/s), which is in excellent agreement with the previous data for undoped bulk samples [76].

The seemingly low intensity near the Dirac point for the doped samples should not be mistaken for the evidence of a gap opening. Rather, it is related to a combination of the low photoemission cross section at the used photon energy of  $h\nu = 21.2$  eV, which is already known for undoped  $\text{Bi}_2\text{Te}_3$  [77], and doping-induced disorder. Indeed, the analysis of energy distribution and momentum distribution curves not shown here provides no evidence of a gap opening.

In Fig. 8(i) we also show a wide energy scan for the 2% sample. The red rectangle highlights the position of the TSS, the CB, and the top of the VB. The VB observed at higher binding energies closely resembles that of the undoped  $\text{Bi}_2\text{Te}_3$ , with no signatures of Eu impurity bands. Here,

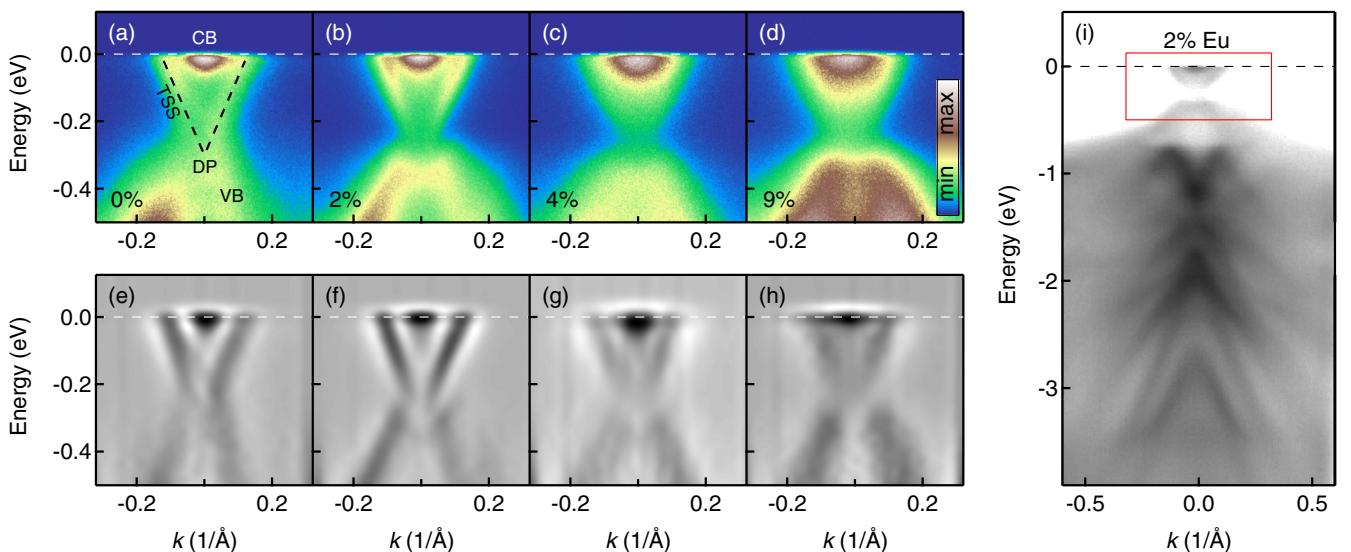


FIG. 8. (a–d) ARPES spectra of Eu-doped  $\text{Bi}_2\text{Te}_3$  thin films with doping ranging from 0% to 9%, measured near the  $\bar{\Gamma}$  point at 20 K using a photon energy  $h\nu = 21.2$  eV. (e–h) Corresponding second derivative plots. (i) Wide-energy-range spectrum near the  $\bar{\Gamma}$  point for the 2% Eu-doped sample.

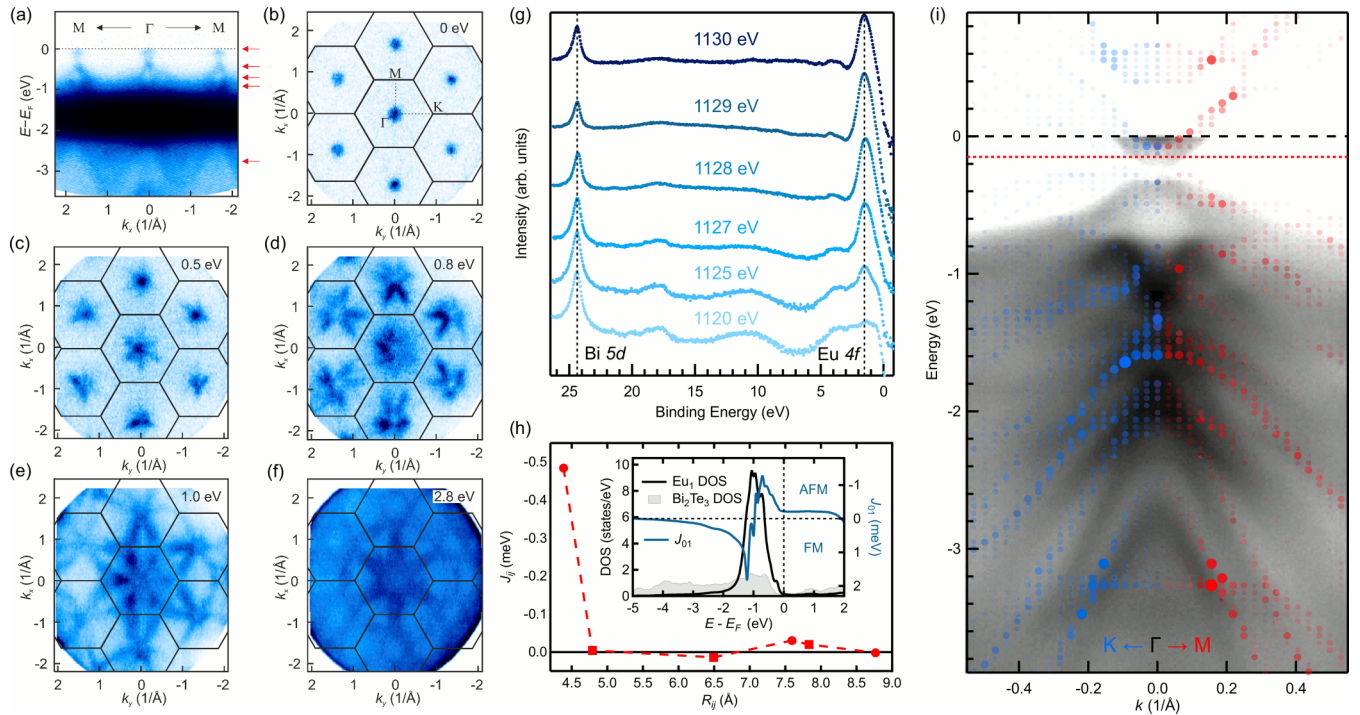


FIG. 9. (a) Energy momentum cut along the  $\bar{\Gamma}\bar{M}$  direction for the 2% sample. (b)–(f) Constant energy maps for binding energies ranging from 0 to 2.8 eV. The hexagonal shapes are the boundaries of the two-dimensional Brillouin zones. (g) ResPES data for the 4% sample showing the Bi  $5d$  and Eu  $4f$  core levels. (h) Distance dependence of the exchange interaction  $J_{ij}$  between pairs of Eu impurities placed in the same (●) or neighboring (■) Bi layers within one quintuple layer. The inset shows  $4f$  dominated total DOS of the Eu dimer (black) and total DOS of the host material (gray) together with the energy dependence of the exchange coupling strength  $J_{01}$  (blue). (i) LDA band structure and ARPES data for the 2% sample. The LDA bands are shown in  $\bar{\Gamma}\bar{M}$  and  $\bar{\Gamma}\bar{K}$  directions with symbols whose size and opaqueness is proportional to the spectral weight. The red dotted line shows the position of the theoretical Fermi level, which differs from the experimental one by 150 meV due to the intrinsic  $n$  doping in the measured sample.

though, one should keep in mind that the photoemission matrix elements may cause a drastic intensity variation between different bands. Under unfavorable conditions, this may result in swamping of a weak impurity signal by a more intense feature.

To conclusively check for the presence of Eu impurity bands, we have performed additional synchrotron-based measurements using different excitation energies. In Fig. 9(a) we show a  $\bar{\Gamma}\bar{M}$  spectrum taken from the 2% sample at 10 K using 265-eV photons. Along with the characteristic Dirac cones and the top of the VB, we now clearly see the impurity band located between 1.1 and 2.25 eV. To better illustrate the dispersion of different features, in Figs. 9(b)–9(f) we also plot several constant energy maps for binding energies ranging from 0 to 2.8 eV. The hexagonal shapes denote the boundaries of the two-dimensional Brillouin zones. Whereas the features seen at the Fermi level around the  $\bar{\Gamma}$  points [Figs. 9(a) and 9(b)] are due to the TSS and the CB, the band structure at higher binding energies outside the region dominated by the impurity bands [Figs. 9(a) and 9(c)–9(f)] is very much like that of typical  $\text{Bi}_2\text{Te}_3$ .

As in the case of V-doped  $(\text{Bi}, \text{Sb})_2\text{Te}_3$  [78], to confirm that the observed flat feature is indeed the Eu  $4f$  impurity band we have performed resPES measurements. Figure 9(g) shows the resPES spectra for the 4% doped sample taken with a photon energy ranging from 1120 to 1130 eV. For photon energies below the resonant one ( $h\nu < 1120$  eV) only the Bi  $5d$  core

level and the valence band are visible. By gradually tuning the photon energy to the Eu  $3d \rightarrow 4f$  resonance, we see a peak growing at around 1.7 eV binding energy. The intensity increase is more than hundredfold, which eventually confirms that the observed feature is the Eu  $4f$  impurity band.

### G. Magnetic exchange coupling calculation

In order to understand the magnetic properties of Eu-doped  $\text{Bi}_2\text{Te}_3$  and the magnetic exchange coupling mechanism between Eu ions, we have performed DFT calculations for bulk-doped  $\text{Bi}_2\text{Te}_3$ , including the effect of correlations within the LDA + U method, as outlined in Sec. IID. The calculated electronic band structure of the host material overlaid with experimental ARPES data is shown in Fig. 9(i). The band dispersion in the  $\bar{\Gamma}\bar{M}$  (red dots) and  $\bar{\Gamma}\bar{K}$  (blue dots) directions shows good agreement with the experimental data.

We find that the occupied  $4f$  states of  $\text{Eu}_{\text{Bi}}$  exhibit a rigid shift down in energy with increasing  $U^{\text{eff}} = U - J$ , which changes the magnetic moment from  $6.58\mu_B$  in the case of pure LDA ( $U = 0, J = 0$ ) to  $6.94\mu_B$  in case of LDA + U ( $U^{\text{eff}} = 8.25$  eV). The size of the magnetic moment and the bandwidth of the  $4f$  states do not change much for  $U^{\text{eff}}$  values ranging from 4.25 to 9 eV, which indicates a stable half-filling of the Eu  $4f$  orbitals and only a weak  $pf$  hybridization with the  $\text{Bi}_2\text{Te}_3$  host system. This is consistent with the very small and antiferromagnetically aligned

induced magnetic moments in the first two Te and the first Bi neighbors around the  $\text{Eu}_{\text{Bi}}$  defect of  $-8.0 \times 10^{-3} \mu_{\text{B}}$ ,  $-4.3 \times 10^{-3} \mu_{\text{B}}$ , and  $-6.9 \times 10^{-5} \mu_{\text{B}}$ , respectively. Additionally, we performed band-structure calculations in a  $2 \times 2 \times 1$  supercell which show that the  $\text{Eu}_{\text{Bi}}$  impurity bands do not disperse due to the weak hybridization of the  $f$  states with its surrounding  $p$  states. This result agrees with the results of the ARPES measurements, see Fig. 9(a).

In Fig. 9(h) we show the distance-dependent exchange coupling constants  $J_{ij}$  for  $U^{\text{eff}} = 8.25$  eV. The inset shows the impurity DOS and the energy-dependent exchange coupling  $J_{01}$  for nearest  $\text{Eu}_{\text{Bi}}\text{-Eu}_{\text{Bi}}$  neighbors ( $R_{ij} = 4.38$  Å) which is in good agreement with the experimentally determined position of the Eu  $4f$  states. We find weak antiferromagnetic interactions for the first-neighbor  $\text{Eu}_{\text{Bi}}$  impurities that are located on the same Bi layer. For larger distance between the Eu atoms the exchange interactions quickly decline. The energy-resolved  $J_{ij}$  reveals a flat plateau of antiferromagnetic interactions above the Fermi level, which increases for smaller  $U^{\text{eff}}$  (not shown). This indicates antiferromagnetic coupling arising from the direct overlap of the impurity wave functions [79,80]. The strong spatial localization of the Eu  $4f$  states explains the weakness of the interaction and the quick decrease with distance.

Additional calculations with a Fermi level shifted into the bulk conduction band show that the strength of the antiferromagnetic exchange interactions can be increased by up to  $\approx 50\%$  for Fermi-level shifts of up to  $\pm 0.4$  eV. However, the weak  $pf$  hybridization between Eu impurity and surrounding host atoms does not result in a significant increase of exchange interactions at larger distances.

#### IV. CONCLUSIONS AND OUTLOOK

Realizing an antiferromagnetic topological insulator by doping  $\text{Bi}_2\text{Te}_3$  with Eu has turned out to be more challenging than realizing its FM counterpart, namely, V- or Cr-doped  $\text{Bi}_2\text{Te}_3$ . One likely reason is the adverse effect of the random—and dilute—impurity distribution on establishing a staggered magnetization.

The disorder and charge doping induced by the nonisoelectronic substitution present another challenge, as they can interfere with the integrity of the TSS. Our comprehensive experimental and theoretical studies indicate that  $\text{Eu}_z\text{Bi}_{2-z}\text{Te}_3$  is not critically affected by these problems. First, the TSS remain detectable in our ARPES results at all Eu concentrations. This is noteworthy, since Eu, unlike most other RE elements, enters  $\text{Bi}_2\text{Te}_3$  as  $\text{Eu}^{2+}$  and thus leads to hole doping and disorder [34].

Second, for all Eu concentrations our SQUID data yield a negative Weiss temperature  $\theta_p$  and a cusplike feature in the  $\chi(T)$  curve, which indicates the onset of antiferromagnetic order for temperatures between 5 and 10 K. Due to the thinness of the samples and the presence of Eu, it was not possible to measure the antiferromagnetic correlation length experimentally using neutron diffraction. However, the antiferromagnetic coupling between Eu atoms is corroborated by our DFT calculations in the LDA + U approximation, which well reproduce our photoemission data. The largest effective  $J_{ij} = -0.5$  meV is found between Eu ions inside the same Bi

layer with its energy comparable to the AFM onset temperature observed in the SQUID data. We point out that previous theoretical studies of  $\text{Eu}_z\text{Bi}_{2-z}\text{Se}_3$  predicted FM order [24], for which we found no evidence in our related telluride system.

Considering the hexagonal arrangement of the atoms in the Bi layer, one would expect the AFM order to get stronger with increasing Eu doping, but then at higher levels increasing frustration should suppress ordering. Counter to this intuition, our SQUID data seem to indicate an increasing AFM onset temperature up to the 9% doping, for which nearly one out of four Bi atoms is replaced by Eu. This is probably due to exceeded Eu solubility in the 9% sample and cluster formation of EuTe [34], which is a well-known antiferromagnet with  $T_N = 9.8$  K.

Whereas in  $\text{MnBi}_2\text{Te}_4$  the interactions are ferromagnetic within the Bi planes and antiferromagnetic between the neighboring planes [26,81], our theoretical prediction of antiferromagnetism in  $\text{Eu}_z\text{Bi}_{2-z}\text{Te}_3$  is different. It closely resembles that found in  $\text{Gd}_z\text{Bi}_{2-z}\text{Te}_3$ , for which DFT calculations yield AFM coupling between Gd atoms inside a Bi plane [32], just like for the Eu atoms in our case. In addition, a gap formation was experimentally observed for Gd doping [33], but its connection to the in-plane AFM interactions still needs to be clarified.

In conclusion, our results warrant further investigations at temperatures below 10 K down to the kelvin range to better understand the character of the antiferromagnetism we observe and to experimentally establish its impact on the TSS. Kelvin-range photoemission and XAS experiments are challenging and were not performed for the present study. Yet, in the light of our results, XAS and dichroism measurements, including linear dichroism to characterize the AFM state, appear promising. Low-temperature ARPES needs to be performed to search for a gap opening in the TSS. The onset of antiferromagnetism over a substantial doping range corroborates the potential of RE doping to result in an AFM topological insulator with exotic quantum properties.

#### ACKNOWLEDGMENTS

We acknowledge financial support by the Deutsche Forschungsgemeinschaft DFG, Project No. 258499086, SFB 1170 (Projects C04, C06 and A01). Further we acknowledge financial support by the Deutsche Forschungsgemeinschaft (DFG) through the Würzburg-Dresden Cluster of Excellence on Complexity and Topology in Quantum Matter ct.qmat (EXC 2147, Project No. 390858490). This work was also supported by the BMBF (Project No. 05K19WW2) and by FAPESP (Grant No. 2016/22366-5). We acknowledge the Diamond Light Source for time on Beamline I10 under Proposal MM19994. We also thankfully acknowledge HZB for the allocation of synchrotron radiation beam time and financial support. Parts of this research was done at PETRA III (DESY, Hamburg, Germany) under Proposal No. I-20181060. We would like to thank F. Diekmann, S. Rohlf, M. Kalläne, and the staff of beamline P04 for experimental support. C.I.F. acknowledges the Hallwachs-Röntgen Postdoc Program of ct.qmat for financial support. P.R. acknowledges support by

the Deutsche Forschungsgemeinschaft (DFG, German Research Foundation) under Germany's Excellence Strategy Cluster of Excellence Matter and Light for Quantum Computing (ML4Q) EXC2004/1, Project No. 390534769. This

work was supported by computing time granted by the JARA Vergabegremium and provided on the JARA Partition part of the supercomputer CLAIX at RWTH Aachen University. We thank B. Katter for support.

- [1] C.-Z. Chang, J. Zhang, X. Feng, J. Shen, Z. Zhang, M. Guo, K. Li, Y. Ou, P. Wei, L.-L. Wang, Z.-Q. Ji, Y. Feng, S. Ji, X. Chen, J. Jia, X. Dai, Z. Fang, S.-C. Zhang, K. He, Y. Wang *et al.*, *Science* **340**, 167 (2013).
- [2] C.-Z. Chang, W. Zhao, D. Y. Kim, H. Zhang, B. A. Assaf, D. Heiman, S.-C. Zhang, C. Liu, M. H. W. Chan, and J. S. Moodera, *Nat. Mater.* **14**, 473 (2015).
- [3] X. Kou, Y. Fan, M. Lang, P. Upadhyaya, and K. L. Wang, *Solid State Commun.* **215-216**, 34 (2015).
- [4] A. J. Bestwick, E. J. Fox, X. Kou, L. Pan, K. L. Wang, and D. Goldhaber-Gordon, *Phys. Rev. Lett.* **114**, 187201 (2015).
- [5] S. Grauer, S. Schreyeck, M. Winnerlein, K. Brunner, C. Gould, and L. W. Molenkamp, *Phys. Rev. B* **92**, 201304(R) (2015).
- [6] D. Xiao, J. Jiang, J.-H. Shin, W. Wang, F. Wang, Y.-F. Zhao, C. Liu, W. Wu, M. H. W. Chan, N. Samarth, and C.-Z. Chang, *Phys. Rev. Lett.* **120**, 056801 (2018).
- [7] S. Grauer, K. M. Fijalkowski, S. Schreyeck, M. Winnerlein, K. Brunner, R. Thomale, C. Gould, and L. W. Molenkamp, *Phys. Rev. Lett.* **118**, 246801 (2017).
- [8] Q. L. He, L. Pan, A. L. Stern, E. C. Burks, X. Che, G. Yin, J. Wang, B. Lian, Q. Zhou, E. S. Choi, K. Murata, X. Kou, Z. Chen, T. Nie, Q. Shao, Y. Fan, S.-C. Zhang, K. Liu, J. Xia, and K. L. Wang, *Science* **357**, 294 (2017).
- [9] M. Sato and Y. Ando, *Rep. Prog. Phys.* **80**, 076501 (2017).
- [10] K. He, Y. Wang, and Q.-K. Xue, *Annu. Rev. Condens. Matter Phys.* **9**, 329 (2018).
- [11] Y. Ou, C. Liu, G. Jiang, Y. Feng, D. Zhao, W. Wu, X.-X. Wang, W. Li, C. Song, L.-L. Wang, W. Wang, W. Wu, Y. Wang, K. He, X.-C. Ma, and Q.-K. Xue, *Adv. Mater.* **30**, 1703062 (2018).
- [12] M. Mogi, R. Yoshimi, A. Tsukazaki, K. Yasuda, Y. Kozuka, K. S. Takahashi, M. Kawasaki, and Y. Tokura, *Appl. Phys. Lett.* **107**, 182401 (2015).
- [13] T. Hesjedal, *Phys. Status Solidi A* **216**, 1800726 (2019).
- [14] S. E. Harrison, L. J. Collins-McIntyre, P. Schönherr, A. Vaillonis, V. Srot, P. A. van Aken, A. J. Kellock, A. Pushp, S. S. P. Parkin, J. S. Harris, B. Zhou, Y. L. Chen, and T. Hesjedal, *Sci. Rep.* **5**, 15767 (2015).
- [15] L. B. Duffy, N.-J. Steinke, J. A. Krieger, A. I. Figueroa, K. Kummer, T. Lancaster, S. R. Giblin, F. L. Pratt, S. J. Blundell, T. Prokscha, A. Suter, S. Langridge, V. N. Strocov, Z. Salman, G. van der Laan, and T. Hesjedal, *Phys. Rev. B* **97**, 174427 (2018).
- [16] S. Li, S. E. Harrison, Y. Huo, A. Pushp, H. T. Yuan, B. Zhou, A. J. Kellock, S. S. P. Parkin, Y.-L. Chen, T. Hesjedal, and J. S. Harris, *Appl. Phys. Lett.* **102**, 242412 (2013).
- [17] A. I. Figueroa, S. E. Harrison, L. J. Collins-McIntyre, G. van der Laan, and T. Hesjedal, *Phys. Status Solidi RRL* **10**, 467 (2016).
- [18] Y. L. Chen, J.-H. Chu, J. G. Analytis, Z. K. Liu, K. Igarashi, H.-H. Kuo, X. L. Qi, S. K. Mo, R. G. Moore, D. H. Lu, M. Hashimoto, T. Sasagawa, S. C. Zhang, I. R. Fisher, Z. Hussain, and Z. X. Shen, *Science* **329**, 659 (2010).
- [19] J. Jensen and A. R. Mackintosh, *Rare Earth Magnetism: Structures and Excitations* (Clarendon Press, Oxford, 1991).
- [20] S. E. Harrison, L. J. Collins-McIntyre, S.-L. Zhang, A. A. Baker, A. I. Figueroa, A. J. Kellock, A. Pushp, S. S. P. Parkin, J. S. Harris, G. van der Laan, and T. Hesjedal, *J. Phys.: Condens. Matter* **27**, 245602 (2015).
- [21] S. E. Harrison, L. J. Collins-McIntyre, S. Li, A. A. Baker, L. R. Shelford, Y. Huo, A. Pushp, S. S. P. Parkin, J. S. Harris, E. Arenholz, G. van der Laan, and T. Hesjedal, *J. Appl. Phys.* **115**, 023904 (2014).
- [22] S. E. Harrison, L. J. Collins-McIntyre, S. L. Zhang, A. A. Baker, A. I. Figueroa, A. J. Kellock, A. Pushp, Y. L. Chen, S. S. P. Parkin, J. S. Harris, G. van der Laan, and T. Hesjedal, *Appl. Phys. Lett.* **107**, 182406 (2015).
- [23] C.-Z. Chang, P. Tang, Y.-L. Wang, X. Feng, K. Li, Z. Zhang, Y. Wang, L.-L. Wang, X. Chen, C. Liu, W. Duan, K. He, X.-C. Ma, and Q.-K. Xue, *Phys. Rev. Lett.* **112**, 056801 (2014).
- [24] B. Deng, Y. Zhang, S. B. Zhang, Y. Wang, K. He, and J. Zhu, *Phys. Rev. B* **94**, 054113 (2016).
- [25] T. Chen, W. Liu, F. Zheng, M. Gao, X. Pan, G. van der Laan, X. Wang, Q. Zhang, F. Song, B. Wang, B. Wang, Y. Xu, G. Wang, and R. Zhang, *Adv. Mater.* **27**, 4823 (2015).
- [26] M. M. Otrokov, I. I. Klimovskikh, H. Bentmann, D. Estyunin, A. Zeugner, Z. S. Aliev, S. Gaß, A. U. B. Wolter, A. V. Koroleva, A. M. Shikin, M. Blanco-Rey, M. Hoffmann, I. P. Rusinov, A. Y. Vyazovskaya, S. V. Ereemeev, Y. M. Koroteev, V. M. Kuznetsov, F. Freyse, J. Sánchez-Barriga, I. R. Amiraslanov *et al.*, *Nature (London)* **576**, 416 (2019).
- [27] R. C. Vidal, H. Bentmann, T. R. F. Peixoto, A. Zeugner, S. Moser, C.-H. Min, S. Schatz, K. Kißner, M. Ünzelmann, C. I. Fornari, H. B. Vasili, M. Valvidares, K. Sakamoto, D. Mondal, J. Fujii, I. Vobornik, S. Jung, C. Cacho, T. K. Kim, R. J. Koch *et al.*, *Phys. Rev. B* **100**, 121104(R) (2019).
- [28] G. Will, S. Pickart, H. A. Alperlein, and R. Nathans, *J. Phys. Chem. Solids* **24**, 1679 (1963).
- [29] E. Schierle, E. Weschke, A. Gottberg, W. Söllinger, W. Heiss, G. Springholz, and G. Kaindl, *Phys. Rev. Lett.* **101**, 267202 (2008).
- [30] H. S. Lee, J. Kim, K. Lee, A. Jelen, S. Vrtnik, Z. Jagličić, J. Dolinšek, and M. H. Jung, *Appl. Phys. Lett.* **107**, 182409 (2015).
- [31] J.-H. Jun, J. Kim, S.-W. Kim, and M.-H. Jung, *Sci. Rep.* **10**, 9615 (2020).
- [32] J. Kim, K. Lee, T. Takabatake, H. Kim, M. Kim, and M.-H. Jung, *Sci. Rep.* **5**, 10309 (2015).
- [33] A. M. Shikin, D. A. Estyunin, Y. I. Surin, A. V. Koroleva, E. V. Shevchenko, K. A. Kokh, O. E. Tereshchenko, S. Kumar, E. F. Schwier, K. Shimada, T. Yoshikawa, Y. Saitoh, Y. Takeda, and A. Kimura, *Sci. Rep.* **9**, 4813 (2019).
- [34] C. I. Fornari, H. Bentmann, S. L. Morelhão, T. R. F. Peixoto, P. H. O. Rappl, A.-V. Tcakaev, V. Zabolotnyy, M. Kamp, T.-L. Lee, C.-H. Min, P. Kagerer, R. C. Vidal, A. Isaeva, M. Ruck, V. Hinkov, F. Reinert, and E. Abramof, *J. Phys. Chem. C* **124**, 16048 (2020).

- [35] C. I. Fornari, P. H. O. Rappl, S. L. Morelhão, T. R. F. Peixoto, H. Bentmann, F. Reinert, and E. Abramof, *APL Mater.* **4**, 106107 (2016).
- [36] C. I. Fornari, P. H. O. Rappl, S. L. Morelhão, and E. Abramof, *J. Appl. Phys.* **119**, 165303 (2016).
- [37] A. Tcakaev, V. B. Zabolotnyy, R. J. Green, T. R. F. Peixoto, F. Stier, M. Dettbarn, S. Schreyeck, M. Winnerlein, R. C. Vidal, S. Schatz, H. B. Vasili, M. Valvidares, K. Brunner, C. Gould, H. Bentmann, F. Reinert, L. W. Molenkamp, and V. Hinkov, *Phys. Rev. B* **101**, 045127 (2020).
- [38] F. De Groot and A. Kotani, *Core Level Spectroscopy of Solids* (CRC Press, Boca Raton, FL, 2008).
- [39] F. de Groot, *J. Electron Spectros. Relat. Phenom.* **67**, 529 (1994).
- [40] J. Viefhaus, F. Scholz, S. Deinert, L. Glaser, M. Ilchen, J. Seltmann, P. Walter, and F. Siewert, *Nucl. Instrum. Methods Phys. Res.* **710**, 151 (2013), The 4th International Workshop on Metrology for X-Ray Optics, Mirror Design, and Fabrication.
- [41] S. Nakajima, *J. Phys. Chem. Solids* **24**, 479 (1963).
- [42] S. H. Vosko, L. Wilk, and M. Nusair, *Can. J. Phys.* **58**, 1200 (1980).
- [43] H. Ebert, D. Ködderitzsch, and D. Minár, *Rep. Prog. Phys.* **74**, 096501 (2011).
- [44] The Jülich KKR Codes (accessed June 10, 2020).
- [45] N. Stefanou, H. Akai, and R. Zeller, *Comput. Phys. Commun.* **60**, 231 (1990).
- [46] N. Stefanou and R. Zeller, *J. Phys.: Condens. Matter* **3**, 7599 (1991).
- [47] R. Zeller, *J. Phys.: Condens. Matter* **16**, 6453 (2004).
- [48] D. S. G. Bauer, Ph.D. thesis, RWTH Aachen University, 2013.
- [49] H. Ebert, A. Perlov, and S. Mankovsky, *Solid State Commun.* **127**, 443 (2003).
- [50] A. Liechtenstein, M. Katsnelson, V. Antropov, and V. Gubanov, *J. Magn. Magn. Mater.* **67**, 65 (1987).
- [51] B. T. Thole, G. van der Laan, J. C. Fuggle, G. A. Sawatzky, R. C. Karnatak, and J.-M. Esteva, *Phys. Rev. B* **32**, 5107 (1985).
- [52] T. Kinoshita, H. P. N. J. Gunasekara, Y. Takata, S.-i. Kimura, M. Okuno, Y. Haruyama, N. Kosugi, K. G. Nath, H. Wada, A. Mitsuda, M. Shiga, T. Okuda, A. Harasawa, H. Ogasawara, and A. Kotani, *J. Phys. Soc. Jpn.* **71**, 148 (2002).
- [53] H. Wada, A. Nakamura, A. Mitsuda, M. Shiga, T. Tanaka, H. Mitamura, and T. Goto, *J. Phys.: Condens. Matter* **9**, 7913 (1997).
- [54] V. Kachkanov, M. J. Wallace, G. van der Laan, S. S. Dhessi, S. A. Cavill, Y. Fujiwara, and K. P. O'Donnell, *Sci. Rep.* **2**, 969 (2012).
- [55] A. Figueroa, A. Baker, S. Harrison, K. Kummer, G. van der Laan, and T. Hesjedal, *J. Magn. Magn. Mater.* **422**, 93 (2017).
- [56] N. A. Anderson, M. Hupaló, D. Keavney, M. C. Tringides, and D. Vahnin, *Phys. Rev. Mater.* **1**, 054005 (2017).
- [57] E. Negusse, J. Dvorak, J. S. Holroyd, M. Liberati, T. S. Santos, J. S. Moodera, E. Arenholz, and Y. U. Idzerda, *J. Appl. Phys.* **105**, 07C930 (2009).
- [58] J. H. Richter, B. J. Ruck, M. Simpson, F. Natali, N. O. V. Plank, M. Azeem, H. J. Trodahl, A. R. H. Preston, B. Chen, J. McNulty, K. E. Smith, A. Tadich, B. Cowie, A. Svane, M. van Schilfgaarde, and W. R. L. Lambrecht, *Phys. Rev. B* **84**, 235120 (2011).
- [59] B. T. Thole, P. Carra, F. Sette, and G. van der Laan, *Phys. Rev. Lett.* **68**, 1943 (1992).
- [60] P. Carra, B. T. Thole, M. Altarelli, and X. Wang, *Phys. Rev. Lett.* **70**, 694 (1993).
- [61] G. van der Laan and B. T. Thole, *Phys. Rev. B* **53**, 14458 (1996).
- [62] C. Kittel and P. McEuen, *Introduction to Solid State Physics*, Vol. 8 (Wiley, New York, 1996).
- [63] R. D. Cowan, *The Theory of Atomic Structure and Spectra* (University of California Press, Berkeley, CA, 1981), Vol. 3.
- [64] S. J. Oh and S. Doniach, *Phys. Rev. B* **26**, 2085 (1982).
- [65] A. B. Shick, L. Havela, A. I. Lichtenstein, and M. I. Katsnelson, *Sci. Rep.* **5**, 15429 (2015).
- [66] G. van der Laan, E. Arenholz, A. Schmehl, and D. G. Schlom, *Phys. Rev. Lett.* **100**, 067403 (2008).
- [67] M. W. Haverkort, M. Zwierzycki, and O. K. Andersen, *Phys. Rev. B* **85**, 165113 (2012).
- [68] R. S. Selinsky, D. J. Keavney, M. J. Bierman, and S. Jin, *Appl. Phys. Lett.* **95**, 202501 (2009).
- [69] T. Kawamoto, K. Fujita, H. Akamatsu, T. Nakamura, T. Kinoshita, M. Mizumaki, N. Kawamura, M. Suzuki, Y. Kususe, S. Murai, and K. Tanaka, *Phys. Rev. B* **88**, 024405 (2013).
- [70] B. Díaz, E. Granado, E. Abramof, P. H. O. Rappl, V. A. Chitta, and A. B. Henriques, *Phys. Rev. B* **78**, 134423 (2008).
- [71] J. M. D. Coey, *Magnetism and Magnetic Materials* (Cambridge University Press, Cambridge, England, 2010).
- [72] K. H. Hellwege, *Einführung in die Festkörperphysik* (Springer-Verlag, Berlin, 2013), Vol. 34.
- [73] L. Kilanski, M. Górska, M. Arciszewska, A. Podgórní, R. Minikayev, B. Brodowska, A. Reszka, B. J. Kowalski, V. E. Slynko, and E. I. Slynko, *Acta Phys. Pol. A* **134**, 950 (2018).
- [74] A. Damascelli, Z. Hussain, and Z.-X. Shen, *Rev. Mod. Phys.* **75**, 473 (2003).
- [75] S. Thirupathiah, T. Stürzer, V. B. Zabolotnyy, D. Johrendt, B. Büchner, and S. V. Borisenko, *Phys. Rev. B* **88**, 140505(R) (2013).
- [76] Y. L. Chen, J. G. Analytis, J.-H. Chu, Z. K. Liu, S.-K. Mo, X. L. Qi, H. J. Zhang, D. H. Lu, X. Dai, Z. Fang, S. C. Zhang, I. R. Fisher, Z. Hussain, and Z.-X. Shen, *Science* **325**, 178 (2009).
- [77] P.-Y. Chuang, S.-H. Su, C.-W. Chong, Y.-F. Chen, Y.-H. Chou, J.-C.-A. Huang, W.-C. Chen, C.-M. Cheng, K.-D. Tsuei, C.-H. Wang, Y.-W. Yang, Y.-F. Liao, S.-C. Weng, J.-F. Lee, Y.-K. Lan, S.-L. Chang, C.-H. Lee, C.-K. Yang, H.-L. Su, and Y.-C. Wu, *RSC Adv.* **8**, 423 (2018).
- [78] T. R. F. Peixoto, H. Bentmann, S. Schreyeck, M. Winnerlein, C. Seibel, H. Maaß, M. Al-Baidhani, K. Treiber, S. Schatz, S. Grauer, C. Gould, K. Brunner, A. Ernst, L. W. Molenkamp, and F. Reinert, *Phys. Rev. B* **94**, 195140 (2016).
- [79] B. Belhadji, L. Bergqvist, R. Zeller, D. P. H., K. Sato, and H. Katayama-Yoshida, *J. Phys.: Condens. Matter* **19**, 436227 (2007).
- [80] P. Rüßmann, S. K. Mahatha, P. Sessi, M. A. Valbuena, T. Bathon, K. A. Kokh, K. Fauth, S. Godey, A. Mugarza, O. E. Tereshchenko, P. Gargiani, M. Valvidares, E. Jiménez, N. B. Brookes, M. Bode, G. Bihlmayer, S. Blügel, P. Mavropoulos, C. Carbone, and A. Barla, *J. Phys. Mater.* **1**, 015002 (2018).
- [81] J. Wu, F. Liu, M. Sasase, K. Ienaga, Y. Obata, R. Yukawa, K. Horiba, H. Kumigashira, S. Okuma, T. Inoshita, and H. Hosono, *Sci. Adv.* **5**, eaax9989 (2019).